ELSEVIER

Journal of Hydrology 263 (2002) 1–22

Journal of Hydrology

www.elsevier.com/locate/jhydrol

Flow and transport in hierarchically fractured rock

Christine Doughty*, Kenzi Karasaki

E.O. Lawrence Berkeley National Laboratory, Earth Sciences Division, University of California, 1 Cyclotron Road, MS 90-1116, Berkeley, CA 94720, USA

Received 8 November 2000; revised 8 November 2001; accepted 14 February 2002

Abstract

We construct multiple realizations of hierarchical fracture networks with fractal dimensions between one and two, then simulate single-well pumping tests and natural-gradient tracer tests on them. We calculate averages and standard deviations of test results over the multiple realizations, and show individual results for selected cases to highlight key features of flow and transport through hierarchically fractured rock. These studies are intended to illustrate the range of possible behavior that can be obtained during fracture-dominated hydraulic and tracer tests, and provide insights into how to interpret field responses. The fractal dimension of the fracture network itself is generally larger than the fractal dimension of the flow field arising during a well test. The performance measures of the natural-gradient tracer tests, including the total flow through the fracture network, tracer travel time, front width, and maximum breakthrough concentration, can all be correlated to fractal dimension. Although some of the features observed in the flow and transport behavior within the hierarchically fractured rock have been observed by other authors using non-fractal fracture network concepts (e.g. channelized flow with early breakthrough times, crossing breakthrough curves), others arise directly from the fractal nature of the fracture network, in which variability occurs on all scales (e.g. front width and maximum breakthrough concentration that are constant over a wide range of fractal dimensions). Generally, transport simulations show large variability within a given realization and among realizations with the same fractal dimension, even in networks whose dimension is close to two. This finding is consistent with the large variability in experimental results observed at fractured rock field sites.

Keywords: Hydrogeology; Fractures; Fractal geometry; Pumping tests; Solute transport; Breakthrough curves

1. Introduction

Hydrogeological problems involving fractured rock are challenging to solve because contrasts in permeability of the fractures and surrounding rock matrix are extreme and localized, making flow strongly dependent on the interconnections between conductive fractures (i.e. the connectivity of the fracture network). Site characterization is difficult because the key features controlling flow are likely to be impossible to identify a priori and they often respond to field tests in ways that are not amenable to simple interpretations (Karasaki, 1987a; National Research Council, 1996, Chapter 5). With the introduction of the concepts of fractal geometry to geological systems (Mandlebrot, 1982; Turcotte, 1992), the notion that fracture networks often have a hierarchical (i.e. fractal) structure has gained support (Sahimi, 1993 and references therein; National Research Council, 1996, Chapter 2 and references therein). In hierarchically fractured rock, both the extent and spacing of fractures vary over a wide range of length scales, which

* Corresponding author. Fax: +1-510-486-4159.
E-mail addresses: cadoughty@lbl.gov (C. Doughty), kkarasaki@lbl.gov (K. Karasaki).

0022-1694/02/$ - see front matter
PII: S0022-1694(02)00032-X

can exacerbate the difficulties associated with understanding flow and transport.

In the present study, we are primarily concerned with the situation that arises when a hierarchically fractured site is encountered in which a small number of wells are available for subsurface characterization. This may occur when multiple sites are under consideration for a particular activity (constructing a geologic nuclear waste repository, for example). It would not be cost effective to drill many wells at many candidate sites, but enough information must be gleaned from each site for good candidates to remain candidates and poor candidates to be eliminated. For a nuclear waste repository site it is critical to develop an understanding of how water flow and radionuclide transport will occur through and away from the repository. Important characterization tools in this regard are pumping tests and tracer tests. In the early stages of site characterization, when only one or a few wells are available, single-well pumping tests are likely to be the primary characterization tool. On the other hand, a natural-gradient tracer test more closely mimics the conditions under which radionuclide escape from a repository is likely to occur and hence provides more reliable characterization information. Such tracer tests require careful design if the results are to be interpretable, making it worthwhile to study the relationships between the responses from single-well pump tests and natural-gradient tracer tests that arise in hierarchically fractured rock.

In a seminal paper, Barker (1988) described how a well test can be used to determine not only the effective transmissivity of a fracture network, but also the dimension of the flow field, which he denotes the generalized radial flow dimension, n. Values of n range from 1 to 3, where the integral values of 1, 2, and 3 correspond to linear, radial, and spherical flow, respectively, and intermediate non-integral values describe flow fields with fractal dimension. Polek (1990) simulated well tests in hierarchical fracture networks with a range of fractal dimensions and found that Barker's generalized radial flow dimension was smaller than the fractal dimension of the fracture network itself. He interpreted this as indicating that flow occurs primarily on a subset of the fracture network, denoted the backbone. In the present paper, we follow a procedure similar to that of Polek but broaden the focus to include transport as well as flow, by simulating natural-gradient tracer tests as well as single-well pumping tests. We examine how fractal dimension affects the performance measures of the natural-gradient tracer tests, including the total flow through the fracture network, tracer travel time, front width, and maximum concentration. Our primary goal is to illustrate the types of flow and transport behavior that are representative of hierarchically fractured rock, and thereby aid the design of field tests and the interpretation of field data.

A number of researchers have used numerical simulations to investigate flow and transport in heterogeneous porous or fractured media (Moreno and Tsang, 1994; Birkhölzer and Tsang, 1997; Berkowitz and Scher, 1997), including several who have explicitly invoked hierarchical concepts (Grindrod and Impey, 1993; Clemo and Smith, 1997). However, none of these authors have systematically investigated how transport processes vary with the fractal dimensions for flow and the fracture network itself, as is done here. Others have investigated the significance of fractal geometry on transport (particularly dispersion) theoretically (Ross, 1986; Cushman, 1991; Tyler and Wheatcraft, 1992 and references therein; Sahimi, 1993 and references therein), providing insightful conceptualizations and elegant mathematical formalisms. The present approach is more practically oriented, with the goal of providing insights and information for designing and interpreting field experiments.

2. Methods

We construct hierarchical fracture networks made up of line segments in two-dimensional (2-D) space (a plane). The networks have fractal dimensions between one and two. For each fractal dimension considered, at least 12 realizations of the fracture network are constructed. We then simulate a single-well pumping test and two natural-gradient tracer tests (with opposite gradients) on each realization. The number of realizations is constrained by available computer resources. In the discussion (Section 4) following presentation of results (Section 3), we demonstrate that the present number of realizations is adequate.

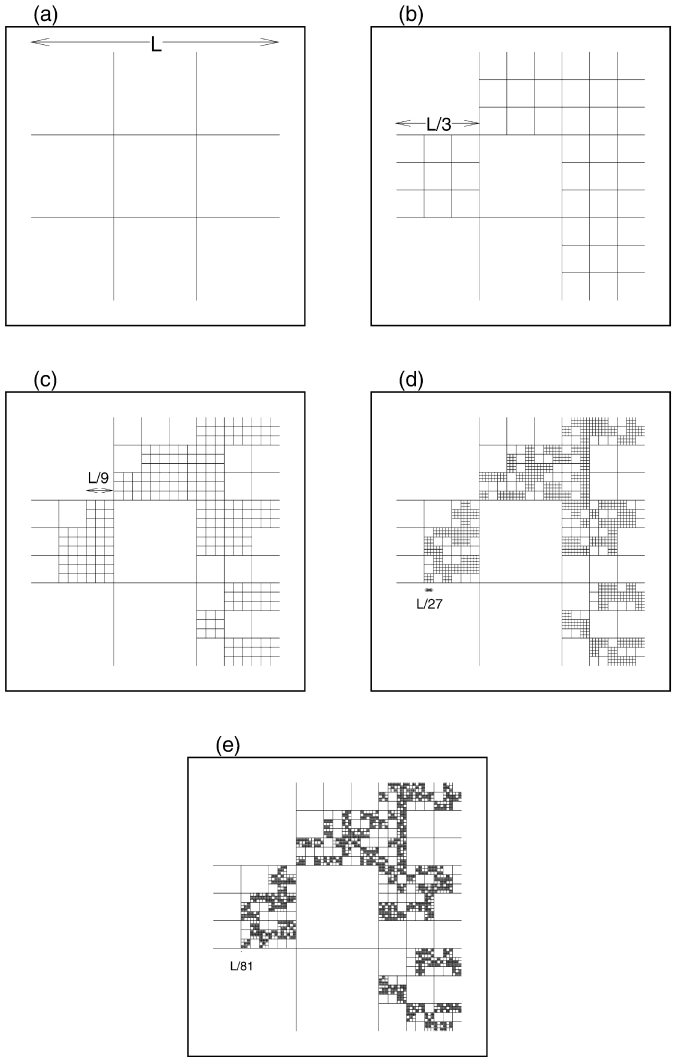

Fig. 1. Construction of a random Sierpinski lattice for $N_{sq} = 5$: (a) the basic template with four fractures of length L, (b) addition of fractures of length $L/3$, (c) addition of fractures of length $L/9$, (d) addition of fractures of length $L/27$, and (e) addition of fractures of length $L/81$.

2.1. Generation of hierarchical fracture networks

The hierarchical fracture networks are generated as random Sierpinski lattices. We begin with a square template consisting of four fractures in two orthogonal sets as shown in Fig. 1(a). This template divides the original square with sides of length L into nine smaller squares, each with sides of length $L/3$. We then shrink the template by a factor of three, replicate it N_{sq} times (where $1 \leq N_{sq} \leq 9$), and superimpose the replicates on the original template in N_{sq} of the nine smaller squares chosen at random, as shown in Fig. 1(b) for $N_{sq} = 5$. This procedure is then repeated for each of the $L/3$-length templates (Fig. 1(c)), then for each of the resulting $L/9$-length and $L/27$-length templates (Fig. 1(d) and (e), respectively). For $1 \leq N_{sq} \leq 8$, the final fracture network contains fractures of length L, $L/3$, $L/9$, $L/27$, and $L/81$, and blocks of intact rock of length $L/3$, $L/9$, $L/27$, $L/81$, and $L/243$. For $N_{sq} = 0$ (the network shown in Fig. 1(a)) and $N_{sq} = 9$, the fracture network is a regular lattice in which all blocks of intact rock have length $L/3$ and $L/243$, respectively.

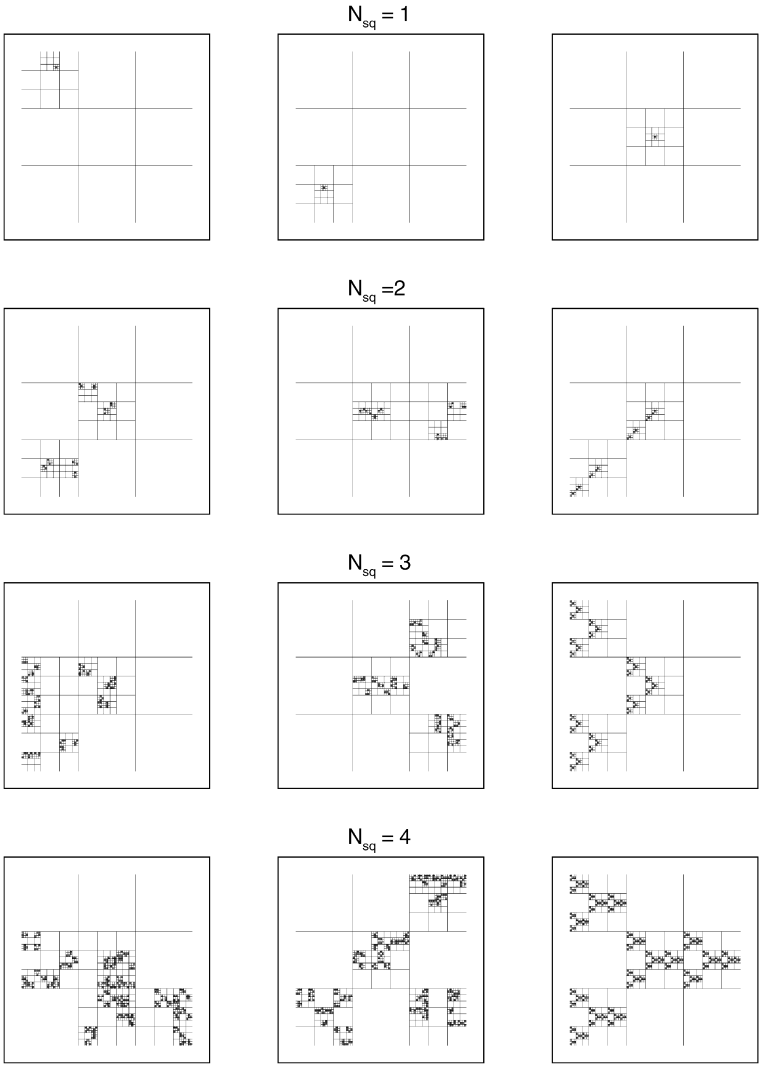

Fig. 2. Some of the fracture networks constructed as random (left and center columns) and regular (right column) Sierpinski lattices.

Fracture networks constructed in this manner are denoted five-level lattices, as they include five sizes of templates. Current computational limitations preclude using higher-level lattices for the present study. In principle, however, we could continue the process, using even smaller templates to represent even smaller fractures until reaching the fractal cutoff length below which fractal geometry is not expected to be the best representation of fracture flow. Fracture mapping studies at The Geysers, California (Sahimi et al., 1993) and Yucca Mountain, Nevada (Barton and Hsieh, 1989) observed fractal geometry over length scale ranges of one and two orders of magnitude, respectively, suggesting that using the five-level lattices, which comprise nearly two orders of magnitude of fracture lengths, is reasonable.

The basic building block of the hierarchical lattices is called a fracture element. It is a fracture segment with a length one-third that of the smallest template used in the lattice. For a lattice with M levels, the smallest template length is $L/3^{M-1}$, therefore the length of a fracture element is $l_{\mathrm{el}} = L/3^{M}$. There are

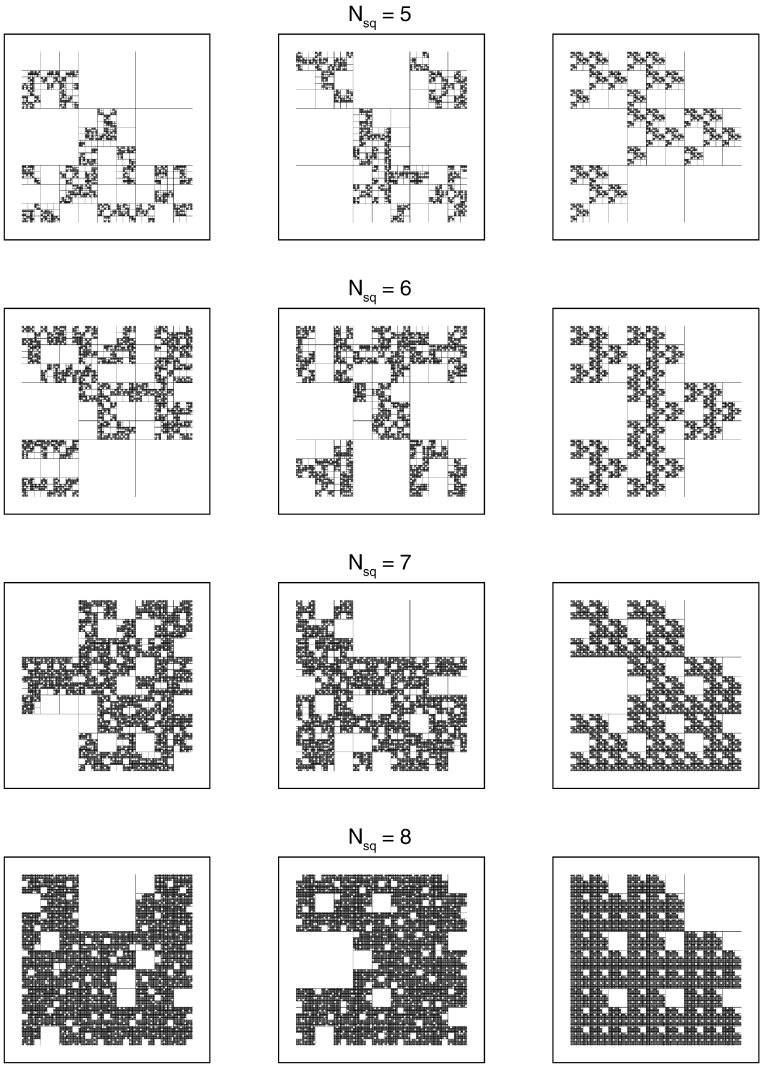

Fig. 2. (*continued*)

12 fracture elements in the smallest templates, and it is straightforward to calculate the total number of fracture elements, denoted N_{el}, in the lattice. First, the total fracture length is obtained by summing the length of fractures added during each level of construction:

$$4L + N_{sq}4L/3 + N_{sq}^2 4L/3^2 + N_{sq}^3 4L/3^3 + \cdots + N_{sq}^{M-1} 4L/3^{M-1} \quad (1)$$

Then, dividing by l_{el} yields N_{el}:

$$N_{el} = 4\left(3^M + N_{sq}3^{M-1} + N_{sq}^2 3^{M-2} + N_{sq}^3 3^{M-3} + \cdots + N_{sq}^{M-1}3\right) = 4(3)^M \sum_{j=0}^{M-1} (N_{sq}/3)^j \quad (2)$$

Applying the summation formula for a geometric

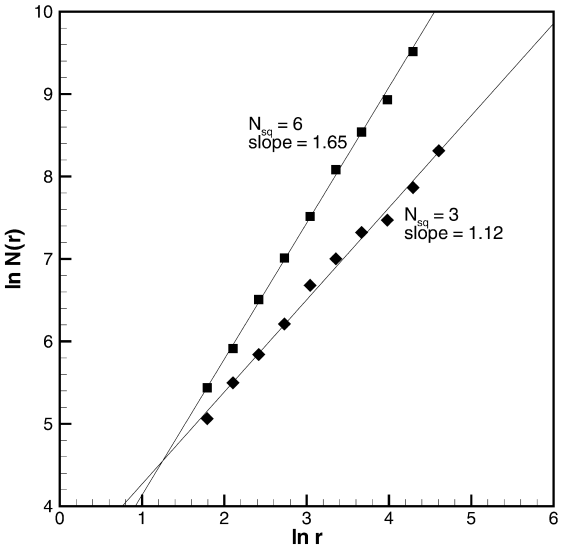

Fig. 3. Example of the box counting method: the symbols show the number of fracture elements $N(r)$ encountered within a radius r of a central point for five-level lattices with $N_{sq} = 3$ and 6. The slope of the best-fit lines is the fractal dimension D of the fracture network.

series yields

$$N_{el} = 4(3)^M \frac{1 - (N_{sq}/3)^M}{1 - (N_{sq}/3)} \tag{3}$$

Fig. 2 shows a selection of the random fracture networks created for each value of N_{sq}. In the lattices shown in the left and center columns of Fig. 2, at each level of construction a different random set of N_{sq} squares is filled with smaller fractures. If the same N_{sq} squares are filled at each level, a much more regular fracture network is formed, as shown in the right column of Fig. 2. We only consider networks containing fractures that pass close to the center of the model (these are picked out randomly from a larger suite of realizations), so that we can compare well tests and tracer tests with a common source location. As N_{sq} decreases for random networks, the probability of a fracture intersecting a given source region becomes smaller and smaller until for $N_{sq} = 1$ there are only a few realizations that do so, all similar to the regular lattice shown in Fig. 2.

The fractal dimension of a fracture network can be determined using the box counting method (Ott, 1993) as shown in Fig. 3, which is a log–log plot of the number of fracture elements $N(r)$ encountered as a

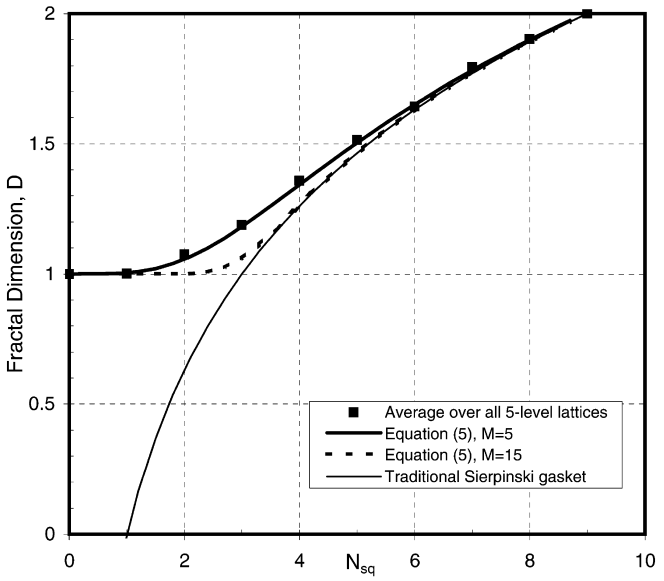

Fig. 4. Fractal dimension D of the fracture network as a function of N_{sq}, with D averaged over at least 12 realizations of five-level lattices for $2 \leq N_{sq} \leq 8$. The fractal dimensions determined from Eq. (5) with $M = 5$ and 15 and that for a traditional Sierpinski gasket in which only the shortest fractures are retained are also shown.

function of distance r from some point in the lattice. The slope of the best-fit line through these points is the fractal dimension, D. Fig. 3 shows $N(r)$ as measured on two five-level lattices with different values of N_{sq}. The good fit to straight lines is typical of all the lattices generated and confirms that five-level fracture networks constructed as shown in Fig. 1 do possess fractal geometry over a range of length scales.

We can derive an analytical expression for $N(r)$, following a line of reasoning similar to that used to derive Eq. (3) for N_{el}, but starting with the smallest template replica ($m = 1$) and subsequently considering larger and larger replicas ($m = 2, 3, \ldots, M$) :

$$N(r) = 4(3)^m \sum_{j=0}^{m-1} (N_{sq}/3)^j = 4(3)^m \frac{1 - (N_{sq}/3)^m}{1 - (N_{sq}/3)}, \quad (4)$$

where r is related to m by $r = l_{el}3^m$. Note that when $r = L, m = M$ and $N(L) = N_{el}$ as defined by Eq. (3). A straightforward calculation yields an expression for the fractal dimension D:

$$D = \frac{\mathrm{d} \ln N(r)}{\mathrm{d} \ln r} = \frac{r}{N(r)} \frac{\mathrm{d}N(r)}{\mathrm{d}r} = \frac{l_{el}3^m}{N(m)} \frac{\mathrm{d}N(m)}{\mathrm{d}m} \frac{\mathrm{d}m}{\mathrm{d}r}$$

$$= \frac{1 - (N_{sq}/3)^m \dfrac{\ln N_{sq}}{\ln 3}}{1 - (N_{sq}/3)^m} \quad (5)$$

For the case $N_{sq} = 3$, Eq. (4) can be simplified before evaluating the sum, yielding

$$N(r) = 4(3)^m m \quad (6)$$

and consequently

$$D = 1 + \frac{1}{m \ln 3} \quad (7)$$

For evaluating the fractal dimension of an M-level lattice, it is appropriate to replace m in Eqs. (5) and (7) with M. The fractal dimensions measured from lattices with $M = 4$ and 5 agree closely with those obtained from the analytical solution using the corresponding values of M, further demonstrating that these lattices adequately capture the desired hierarchical structure.

Fig. 4 shows D averaged over all realizations of the five-level lattices as a function of N_{sq}. Also shown is D as given by Eqs. (5) and (7) with $M = 5$ (to compare to the average values) and $M = 15$ (to represent a more idealized hierarchical medium beyond our present numerical capabilities).

Note that as M gets very large, Eqs. (5) and (7) become

$$D \approx \frac{\ln N_{sq}}{\ln 3} \qquad \text{for } N_{sq} > 3, \quad (8)$$

$$D \approx 1 \qquad \text{for } N_{sq} \leq 3. \quad (9)$$

Eq. (8) is the fractal dimension of a traditional Sierpinski gasket; it is also plotted in Fig. 4. In contrast to the present algorithm for fracture network generation, which retains fractures of all lengths, the traditional Sierpinski gasket retains only the smallest ones, i.e. those resulting from the final shrinkage, replication, and superposition of the template. When $N_{sq} \leq 3$, the number of shorter fractures grows slowly as the lattice is generated and the original long fractures contribute significantly to the fractal dimension. In contrast, when $N_{sq} > 3$, the reverse is true and Eq. (8) holds even for modest values of M.

Although they are highly idealized, we believe that the hierarchical fracture networks generated as random Sierpinski lattices are useful for representing real fractured rock for the following reasons. Most importantly, fractures of all lengths are present and blocks of intact rock matrix of all sizes are present. For low values of N_{sq}, fracturing is generally sparse, with only a few through going paths. In contrast, for higher values of N_{sq}, fracturing is ubiquitous whereas gaps in the fracture network are sparse. Under both conditions, there is a huge variability among realizations, as is seen in nature. Finally, the fractures form two orthogonal sets, another feature commonly seen in field settings. A possible limitation is that we are guaranteed to have long continuous fractures with a regular geometry (the tick-tack-toe pattern of the basic template). For low values of N_{sq}, this may dominate behavior.

In the present work, all fractures have the same transmissivity ($T = 10^{-7}$ m^2/s), a simplification that allows us to focus on the fracture network geometry. This treatment should be adequate when variability in fracture transmissivity is relatively small or is not correlated to fracture length. The more complicated case in which fracture transmissivity is correlated

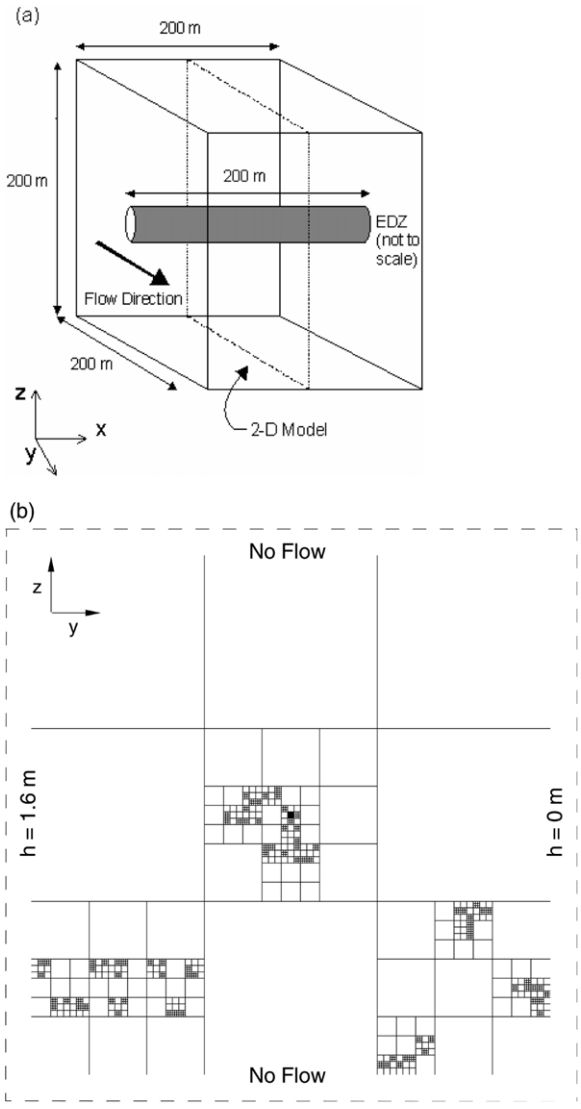

Fig. 5. Schematic of the H-12 problem: (a) full 3-D problem, and (b) 2-D slice through the center of the block modeled in the present studies. The EDZ is shown as a solid black square in the center. For tracer tests with a reverse gradient, the flow direction arrow in (a) is reversed and $h = -1.6$ m on the left boundary in (b).

with fracture length is described elsewhere (Doughty and Karasaki, 2000).

For the flow calculations, fracture aperture w and transmissivity T are assumed to be related according to the cubic law (i.e. w is the hydraulic aperture). For the transport calculations, the tracer aperture is assumed to be 10 times larger than the hydraulic aperture, to account for fracture roughness. The factor of 10 is taken from calibration of a numerical model to data from a tracer test conducted in a fractured rock (Uchida and Sawada, 1995). How generally applicable this factor is remains unknown. However, its only role in the present study is as a multiplicative scale factor for tracer velocity (i.e. tracer moves 10 times more slowly through a 10 times wider fracture so breakthrough times are 10 times longer than they would be if the hydraulic aperture were used); it does not affect the dependence of transport behavior on fractal geometry.

2.2. Flow and transport simulator

The finite element model TRIPOLY (Karasaki, 1987b; Segan and Karasaki, 1993; Birkhölzer and Karasaki, 1996) is used to simulate water flow and tracer transport through the hierarchical fracture networks. Fractures are represented as one-dimensional linear elements and fracture intersections are represented as nodes. A special-purpose grid generator is used to create the hierarchical lattices described in Section 2.1. TRIPOLY models transient or steady flow according to Darcy's law and models transport using the advection–dispersion equation (ADE). Transport calculations use a mixed Lagrangian–Eulerian scheme combined with an adaptive gridding algorithm that places additional nodes in locations of large concentration changes to minimize the numerical dispersion. Complete mixing is assumed at fracture intersections. For the present transport calculations, we neglect diffusion and dispersion within individual fractures because sensitivity studies have shown that it has only a small effect compared to the mixing and dispersion that arise from the highly irregular flow field that develops in the complicated hierarchical fracture networks.

2.3. Single-well pumping test analysis

Barker (1988) generalized the diffusion equation for radial liquid flow to non-integral flow dimensions, in order to analyze data from well tests conducted in fractured rock. He obtained an analytical expression for the transient drawdown during a constant-rate pumping test in terms of the (complementary) incomplete gamma function (Barker, 1988; Press et al., 1986). The expression includes a parameter ν that is

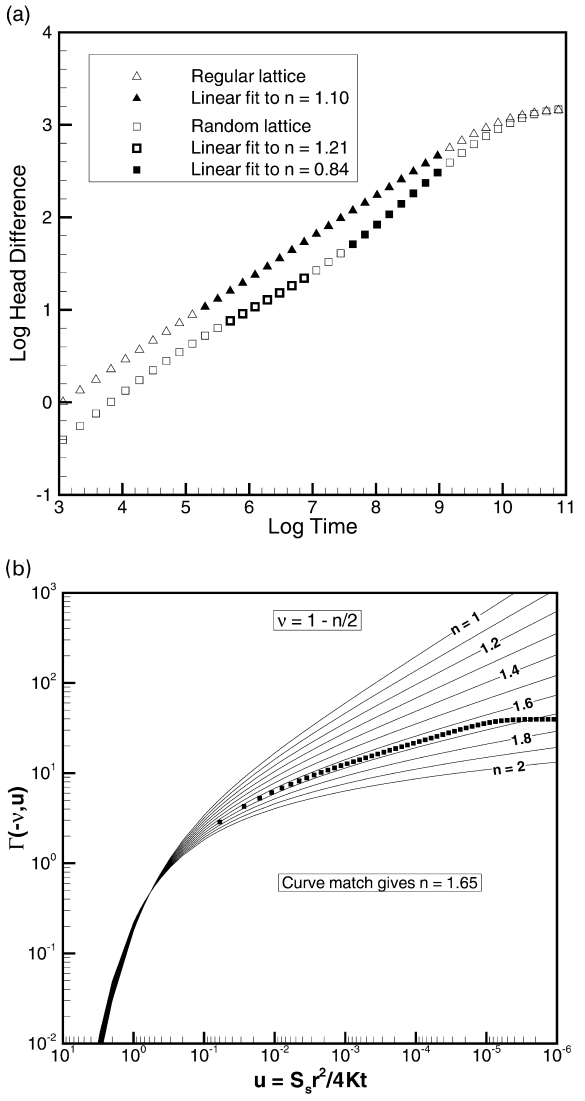

Fig. 6. Numerically simulated drawdown for single-well constant-rate pumping tests for lattices with: (a) $N_{sq} = 3$, and (b) $N_{sq} = 7$. The late-time leveling out of drawdown represents the pressure pulse reaching the outer boundary of the model, and is not used in the matching process. In (b) Barker's (1988) analytical solution in terms of the incomplete gamma function is also shown; in dimensionless time u, S_s and K are the specific storage and hydraulic conductivity, respectively, of the fracture network and r is the radius of the pumping well.

related to the generalized radial flow dimension n according to $\nu = 1 - n/2$. For $n = 2$, the incomplete gamma function simplifies to the familiar exponential integral of the Theis (1935) equation. For $n < 2$, the slope of the log drawdown–log time plot becomes linear at long times, with a slope given by ν. We numerically simulate single-well, constant-rate pumping tests by applying a mass sink to nodes near the center of the lattice while holding nodes along the outer boundary of the lattice at constant hydraulic head. Comparing the resulting transient drawdown to the analytical solution provides an estimation of n. For small values of n, the linear late-time slope provides a simple way to estimate n, but for larger values of n, the constant-head outer boundary of the lattice is felt before the drawdown curve becomes linear, requiring that the complete curve (prior to boundary effects being felt) be matched.

2.4. Natural-gradient tracer test analysis

The Japan Nuclear Cycle Development Institute (JNC) recently conducted a multi-national project to investigate the uncertainties involved in the prediction of the flow and transport behavior of a fractured rock mass (Oyamada and Ikeda, 1999; Sawada et al., 1999; Doughty and Karasaki, 1999). In that project, known as the H-12 flow comparison, several research organizations conducted numerical simulations of radionuclide transport away from a repository under the influence of a uniform horizontal head gradient (essentially, a long-term natural-gradient tracer test). For the present studies, we consider the same geometry as the H-12 problem and evaluate similar performance measures, but consider flow and transport through hierarchical fracture networks.

The H-12 problem involves a 200 m × 200 m × 200 m cube of granitic rock containing a 200 m long, 2.2 m diameter cylindrical gallery, located in the middle of the volume (Fig. 5(a)). The surface of the cylindrical gallery is a no-flow boundary condition (to represent an engineered barrier). The gallery is surrounded by an annular excavation-damaged zone (EDZ) with a thickness of 0.5 m and a low permeability. Heads are assumed uniform on both x–z boundary planes and the head difference between the two planes is 1.6 m. No-flow boundary conditions are assumed for all the x–y and y–z boundary planes. Hence, flow is generally perpendicular to the gallery (along the y-axis).

For the present studies, we consider a 2-D slice

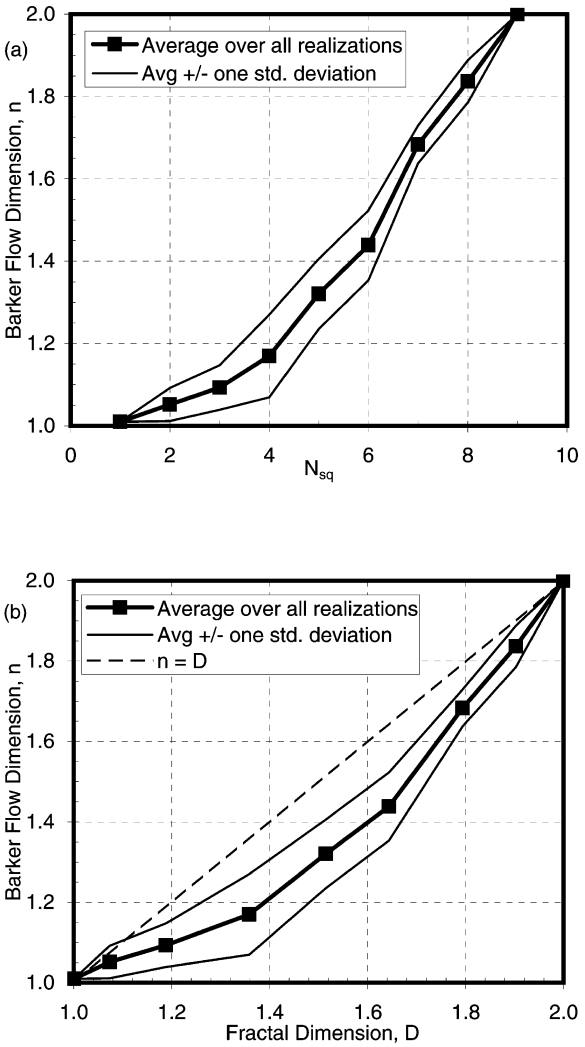

Fig. 7. Generalized radial flow dimension n as a function of: (a) N_{sq} and (b) D.

through the middle of the granite cube in the y–z plane (Fig. 5(b)). For simplicity, the EDZ is modeled as a 2.5 m × 2.5 m square region in which all elements have a low transmissivity ($T = 5 \times 10^{-10}$ m^2/s). The EDZ size equals the smallest size to which the original four-fracture template (Fig. 1(a)) is reduced ($200/3^4$ m on a side). The corner nodes of the EDZ are maintained at a constant tracer concentration $C = 1$ to represent the potential escape of radionuclides from the EDZ.

The H-12 performance measures that we examine are

- Q, the steady-state flow rate through the model (i.e. discharge per unit width in m^2/s), which can be converted to the effective transmissivity of the fracture network,
- Q_{EDZ}, the steady-state flow rate through the EDZ, which influences the quantity of radionuclides released, and ultimately the integrity of the gallery itself,
- t_{bt}, the fastest tracer travel time from the EDZ to the downgradient boundary of the model.

In addition, we monitor C_{max}, the maximum concentration at the downgradient boundary of the model and Δt, the width of the concentration front at the location where C_{max} occurs. Furthermore, we can convert Δt (the front width in time) to Δy (the front width in space) by multiplying Δt by the average velocity of the front, $L/(2t_{bt})$, where $L/2$ is the distance from the EDZ to the downgradient boundary of the model, 100 m. Then Δy may be used as a measure of the effective dispersion occurring in the fracture network.

3. Simulation results

We examine well-test (flow) and tracer-test (flow and transport) simulation results by calculating averages and standard deviations over the multiple realizations. We also show individual simulation results for selected cases to illustrate key features of flow and transport through hierarchically fractured rock.

3.1. Flow

Fig. 6 shows some examples of the numerically simulated drawdown response at the pumping well for single-well constant-rate pumping tests in hierarchical fracture networks. In Fig. 6(a), the generalized radial flow dimension n is determined from the late-time slope ν of the log drawdown-log time plot ($\nu = 1 - n/2$) for two realizations with $N_{sq} = 3$. Some fracture networks produce late-time drawdowns that show distinctive breaks in slope, indicating subregions with different flow dimensions. Fig. 6(b)

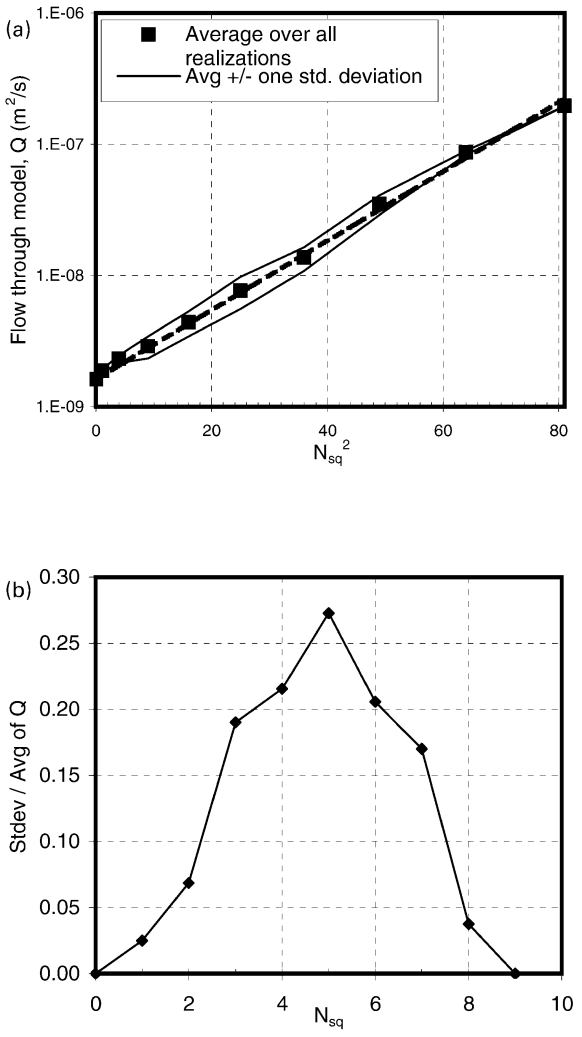

Fig. 8. Flow through the fracture network during a natural-gradient tracer test: (a) average Q as a function of N_{sq}^2, and (b) standard deviation of Q divided by average Q as a function of N_{sq}.

compares the entire drawdown curve for an $N_{sq} = 7$ lattice with Barker's analytical solution, indicating that the flow dimension for this network is about $n = 1.65$. We estimate flow dimensions for all the realizations of hierarchical lattices for each N_{sq} value using one of these two methods and calculate the arithmetic average and standard deviation, which are plotted versus N_{sq} in Fig. 7(a). Note that plotting average plus or minus standard deviation does not imply that the underlying distributions are normal or even symmetric. It just provides a convenient means of illustrating the variability between realizations.

Combining the n versus N_{sq} plot (Fig. 7(a)) with the D versus N_{sq} plot (Fig. 4) yields a plot of flow dimension n versus fractal dimension D (Fig. 7(b)), which shows that $n < D$ for all N_{sq}. Following Polek (1990), we interpret this as indicating that flow occurs primarily on a 'backbone' portion of the fracture network. It is important to realize that no dead-end fractures exist in the hierarchical fracture networks by virtue of their construction as random Sierpinski lattices. Hence, our usage of the term backbone is distinct from the common network or percolation theory usage in which the backbone contains all conductive (i.e. non-dead-end) fractures.

Fig. 8(a) shows the steady linear flow rate Q through the fracture network during the simulation of the H-12 tracer test. For $2 \leq N_{sq} \leq 8$, the values of Q represent an average over at least 12 realizations (for $N_{sq} = 9$ there is only one realization possible, and for $N_{sq} = 1$ there is only one realization in which fractures pass through the center of the model). The relationship between Q and N_{sq} can be reasonably well fit with the expression

$$Q = Q_0 \exp[(N_{sq}/4)^2], \tag{10}$$

where Q_0 is the flow through the basic tick-tack-toe pattern (Fig. 1(a)) that corresponds to $N_{sq} = 0$. With the H-12 boundary conditions specifying a fixed head gradient ∇h, Q is easily converted into the effective transmissivity of the fracture network T_{eff}:

$$Q = -T_{eff} \nabla h. \tag{11}$$

For $N_{sq} = 0$, we have

$$Q_0 = -T_0 \nabla h, \tag{12}$$

where $T_0 = 2 \times 10^{-7}$ m^2/s is the network transmissivity for $N_{sq} = 0$ (two parallel fractures, each with a transmissivity of 10^{-7} m^2/s).

Thus

$$T_{eff}/T_0 = Q_{eff}/Q_0 = \exp[(N_{sq}/4)^2], \tag{13}$$

and finally

$$\ln(T_{eff}/T_0) = (N_{sq}/4)^2. \tag{14}$$

Given the smooth relationships between N_{sq}, D, and n (Fig. 7), we could fit curves to $D(N_{sq})$ and $n(N_{sq})$ and

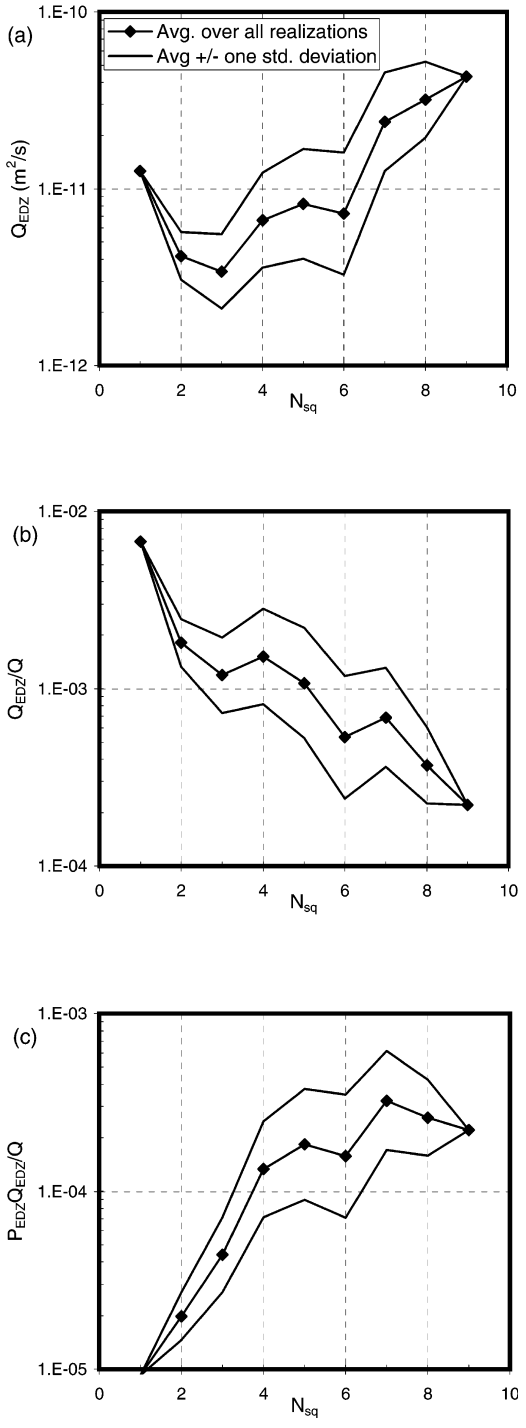

Fig. 9. Different ways of evaluating flow through the EDZ during a tracer test: (a) Q_{EDZ} versus N_{sq}, (b) Q_{EDZ}/Q versus N_{sq}, (c) $P_{EDZ}Q_{EDZ}/Q$ versus N_{sq}.

hence express T_{eff}/T_0 as a function of D or n as well. Note that during the well tests, as N_{sq} increases the generalized radial flow dimension n increases, with T remaining constant. In contrast, during the tracer tests the flow dimension remains one, as it is controlled by the constant head boundary conditions, and T_{eff} increases with N_{sq} as shown in Eq. (14).

Fig. 8(b) shows the standard deviation of Q divided by the average Q. It features a maximum for intermediate values of N_{sq}, indicating that a greater variety of flow fields occur for intermediate values of N_{sq}. This is simply a consequence of the greater variety of fracture networks that can be constructed under these conditions.

Fig. 9(a) shows the average and standard deviation over all realizations for Q_{EDZ}, the flow rate passing through the EDZ during the tracer test. Q_{EDZ} generally increases with N_{sq}, as does the total flow through the fracture network Q (Fig. 8), but the standard deviation of Q_{EDZ} is much larger than that of Q, indicating larger variability between realizations. This greater variability is reasonable, as Q and n embody integration over all the flow paths through the fracture network, whereas Q_{EDZ} depends strongly on the particular flow paths intersecting the EDZ. Another way to look at EDZ flow is to plot Q_{EDZ}/Q versus N_{sq}, as shown in Fig. 9(b). We see an overall decrease with N_{sq}, indicating that as more alternative flow paths become available, more flow bypasses the EDZ. Note that dividing by Q is equivalent to considering fracture networks that have the same T_{eff} regardless of N_{sq}. From a well-testing point of view this may be the most common situation to find in practice. Recall that the realizations used for each N_{sq} were chosen specifically so that the fracture network would intersect the EDZ. We can combine the probability that the fracture network intersects the EDZ (P_{EDZ}) and EDZ flow by plotting $P_{EDZ}Q_{EDZ}/Q$ versus N_{sq} (Fig. 9(c)), which shows an increase for low N_{sq} followed by a plateau for higher values. For small N_{sq} values, the small probability of the fracture network intersecting the EDZ dominates but for large N_{sq} values, the probability flattens out and nearly balances the decrease that occurs as more alternative flow paths are added.

3.2. Transport

To compare transport through the hierarchical

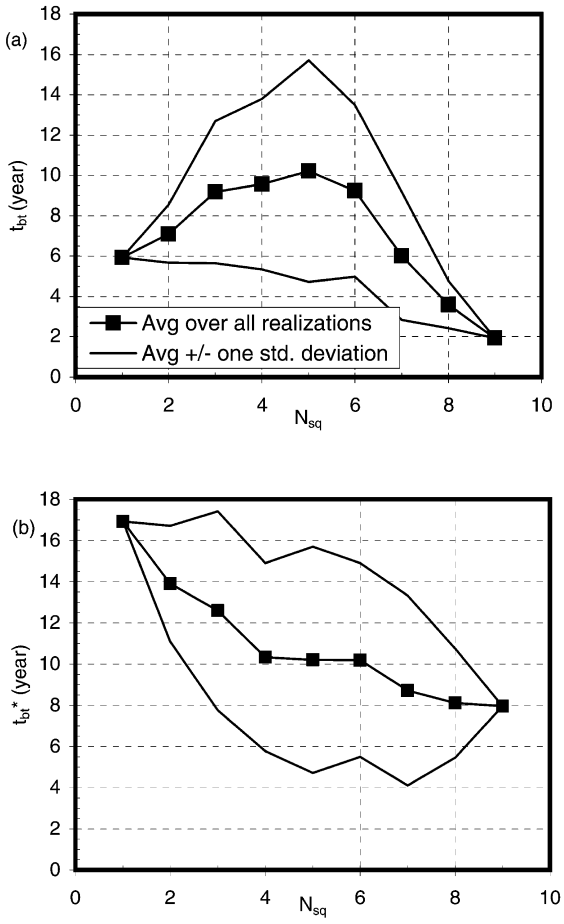

Fig. 10. Breakthrough time at the downgradient boundary of the model as a function of N_{sq}: (a) actual breakthrough time t_{bt}, and (b) normalized breakthrough time t_{bt}^*, with the influence of effective network transmissivity and total void space removed.

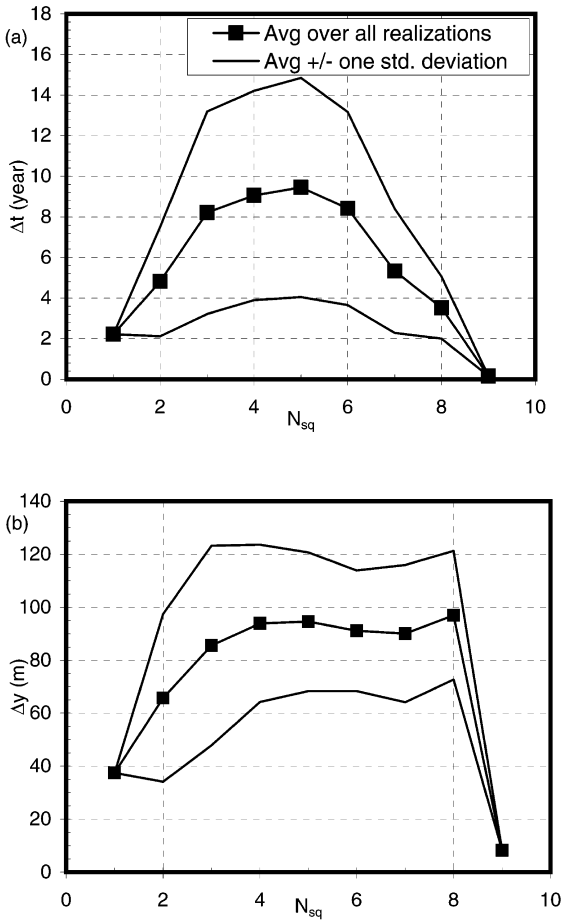

Fig. 11. Concentration front width at the downgradient boundary of the model as a function of N_{sq}: (a) front width in time Δt, and (b) front width in space Δy.

fracture networks we identify the location along the downgradient boundary of the model where the maximum concentration C_{max} occurs for each simulation. For this location, we define the breakthrough time t_{bt} as the time at which the concentration reaches $C_{max}/2$ and the width of front Δt as the time over which the concentration increases from 0 to C_{max}. These quantities are averaged over at least 24 simulations (at least 12 fracture network realizations, each with tracer tests in two directions) and plotted as a function of N_{sq} (Figs. 10(a), 11(a), and 12).

Fig. 10(a) shows that as N_{sq} increases, t_{bt} increases initially then decreases. The addition of flow paths with increasing N_{sq} enlarges both T_{eff} (Eq. (13)) and the total void space of the fracture network. On average, increases in T_{eff} would be expected to shorten t_{bt} whereas increases in void space would lengthen t_{bt}. However, for a hierarchical fracture network, with its highly irregular manner of filling space, individual tracer flow paths can be affected in a wide range of ways by the introduction of additional flow paths, depending on the details of the connectivity of the fracture network. The variation in Fig. 10(a) suggests that at low values of N_{sq}, increasing the number of flow paths provides additional void space but not much additional connectivity, so t_{bt} increases. Essentially the reverse is true at high values of N_{sq}, where the addition of just a few flow paths may provide

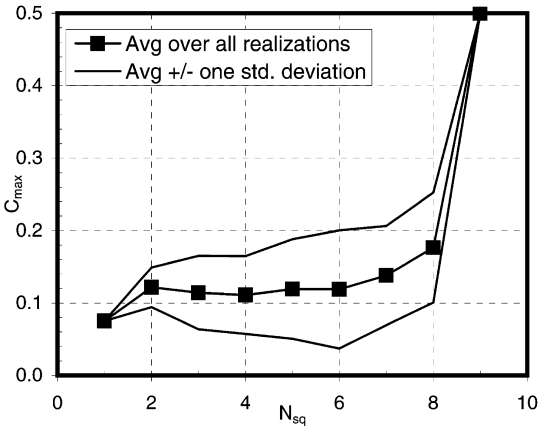

Fig. 12. Maximum concentration at the downgradient boundary of the model as a function of N_{sq}.

much more direct connections across the model, greatly decreasing t_{bt}.

Another way to compare breakthrough times for different N_{sq} values is to normalize t_{bt} by T_{eff} and the total void space of the lattice, as shown in Fig. 10(b). Normalizing t_{bt} is equivalent to assuming that for each value of N_{sq}, the transmissivity and aperture of the individual fractures are chosen such that the effective transmissivity and total void space of the model remain constant. In a sense, this normalization isolates fractal geometry effects from other influences. Normalized time t^*_{bt} is defined as

$$t^*_{bt} = t_{bt} \frac{Q(N_{sq})}{Q(5)} \frac{N_{el}(5)}{N_{el}(N_{sq})}, \tag{15}$$

where $N_{sq} = 5$ is arbitrarily chosen as the reference value for which $t_{bt} = t^*_{bt}$. There is a general decline in t^*_{bt} as N_{sq} increases, suggesting that the additional flow paths introduced for higher fractal geometry provide more direct routes for tracer travel through the model.

Just as converting t_{bt} to t^*_{bt} serves to isolate the effects of fractal geometry, so does converting front width in time Δt (Fig. 11(a)) to front width in space Δy (Fig. 11(b)). For small values of N_{sq}, few alternative flow paths are available so Δy is small. For $N_{sq} = 9$, only the most direct flow path need be taken, again yielding small Δy. For $3 \le N_{sq} \le 8$, Δy is roughly constant and approximately equal to the distance traveled, $L/2$. For some of the tracer test simulations, $C(t)$ curves are available at a series of distances y from the EDZ along the path of peak concentration. At each distance, Δt can be converted to Δy, which is then plotted versus y (not shown). There is a good deal of scatter between realizations (as in Fig. 11(b)) but on average the trend of $\Delta y \approx y$ is maintained for all values of N_{sq} between 3 and 8. The lack of dependence of Δy on N_{sq} (or equivalently on D or n) appears to be a fundamental result for these hierarchical fracture networks and is further discussed in Section 4.

The maximum concentration arriving at the downgradient boundary of the model (Fig. 12) is quite low compared to the constant concentration ($C = 1$) maintained at the EDZ. This is because the EDZ is located away from the long through-going fractures of the full-size template and there is rarely a direct path across the model that intersects the EDZ but misses these long fractures, which contribute clean water from the upgradient boundary of the model. C_{max} shows only a gradual increase with N_{sq}, until $N_{sq} = 9$. Apparently even for the large N_{sq} values of seven and eight, where we might expect that a direct path from the EDZ to the downgradient model boundary would result in a large C_{max}, the occasional presence of large gaps in the fracture network is sufficient to disorganize the flow pattern, enabling mixing to reduce C_{max}.

The standard deviations tend to be very large for parameters that reflect preferential flow through one or only a few flow paths: Q_{EDZ}, t_{bt}, Δt, and C_{max} (Figs. 9–12). This illustrates the basic difficulty of attempting to obtain meaningful results by averaging over multiple realizations for any quantity which itself is not representative of average behavior within a given realization. It makes more sense to consider the range of results possible for different realizations than to focus on the averages themselves.

It is apparent from Figs. 10–12 that the standard deviations of t_{bt}, Δt, and C_{max} all show peaks at intermediate values of N_{sq}, as seen for Q (Fig. 8(b)). This decrease in predictability arises because intermediate values of N_{sq} (or equivalently fractal dimensions midway between one and two) have the widest range of possibilities for connectivity of the fracture network. For n or D close to one, there is rarely more than one flow path between any two points and for n or D close to two, there are generally many paths. In contrast, for intermediate values of n or D, there could

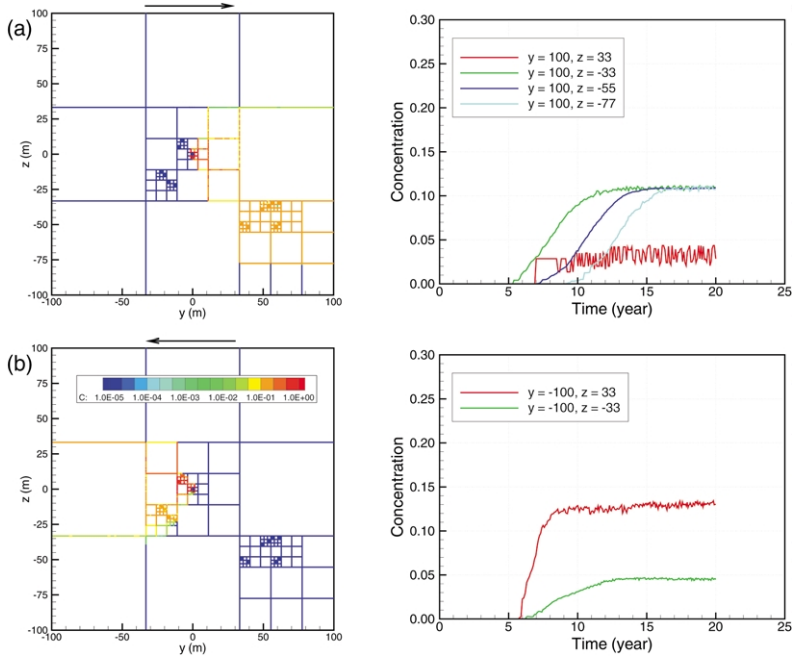

Fig. 13. Steady-state concentration distribution and breakthrough curves at selected points on the downgradient boundary for an $N_{sq} = 2$ lattice. The arrows identify the overall flow

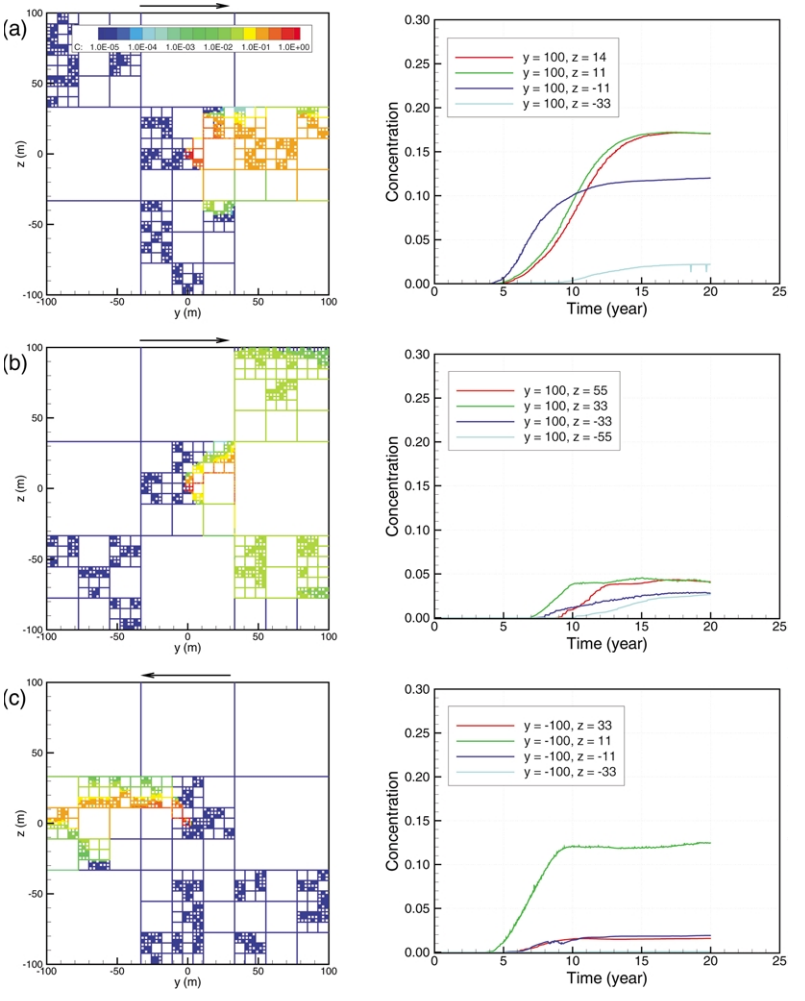

Fig. 14. Steady-state concentration distribution and breakthrough curves at selected points on the downgradient boundary for $N_{sq} = 4$ lattices.

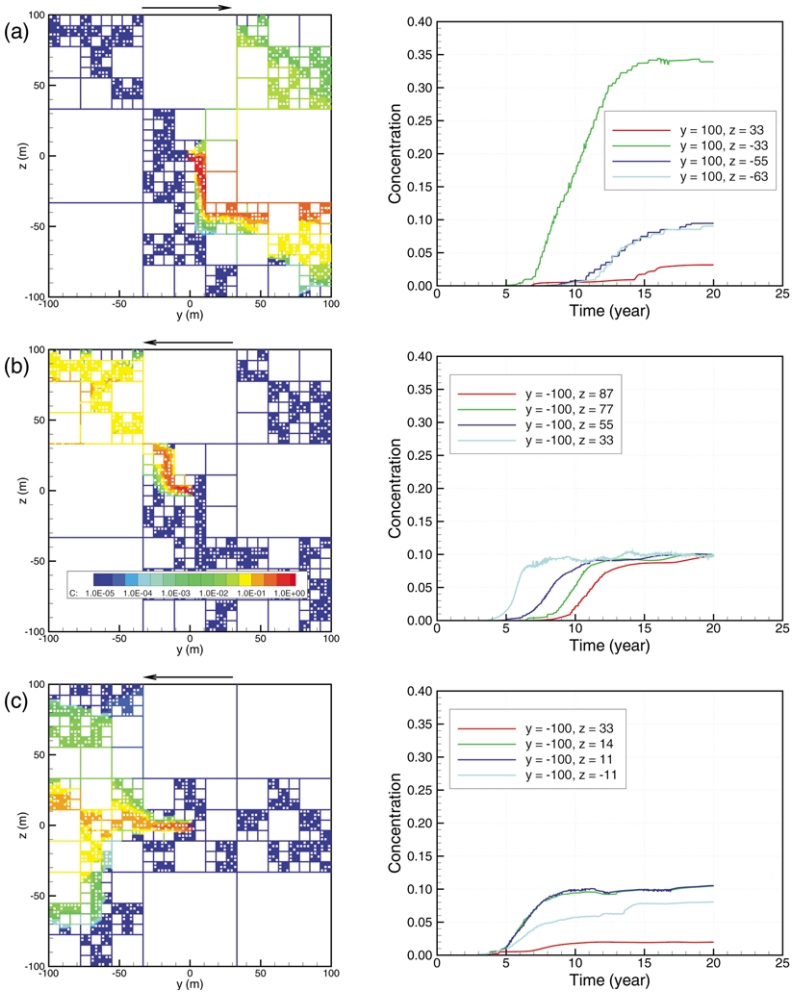

Fig. 15. Steady-state concentration distribution and breakthrough curves at selected points on the downgradient boundary for $N_{sq} = 5$ lattices.

be any number of flow paths and hence a wide range of flow and transport behavior must be expected.

Figs. 13–16 show steady-state concentration distribution, $C(y, z)$, and transient breakthrough curves, $C(t)$, for various values of N_{sq} to illustrate some of the key features of flow and transport in hierarchically fractured rock. For small values of N_{sq}, the situation shown in Fig. 2 for $N_{sq} = 2$ and 3 is typical in that at least one of the constant head boundaries is intersected by only two long fractures. If this is the upgradient boundary of the model, then flow through the EDZ tends to have a diverging character, as shown in Fig. 13(a) for $N_{sq} = 2$. Conversely, if the downgradient boundary of the model intersects only two long fractures, then all flow through the EDZ must ultimately converge into these two fractures (Fig. 13(b)). These different flow distributions produce sharply different breakthrough curves. Tracer moving through the diverging flow fields passes through many fracture intersections, resulting in much mixing and spreading, resulting in classical S-shaped breakthrough curves with late breakthrough times (exemplified by the breakthrough curves for $z < 0$ in Fig. 13(a)). Converging flow occurs along fewer flow paths, leading to earlier, sharper breakthrough curves (Fig. 13(b)).

Within an overall diverging flow field there are often ‘pinch points,’ where flow through a network

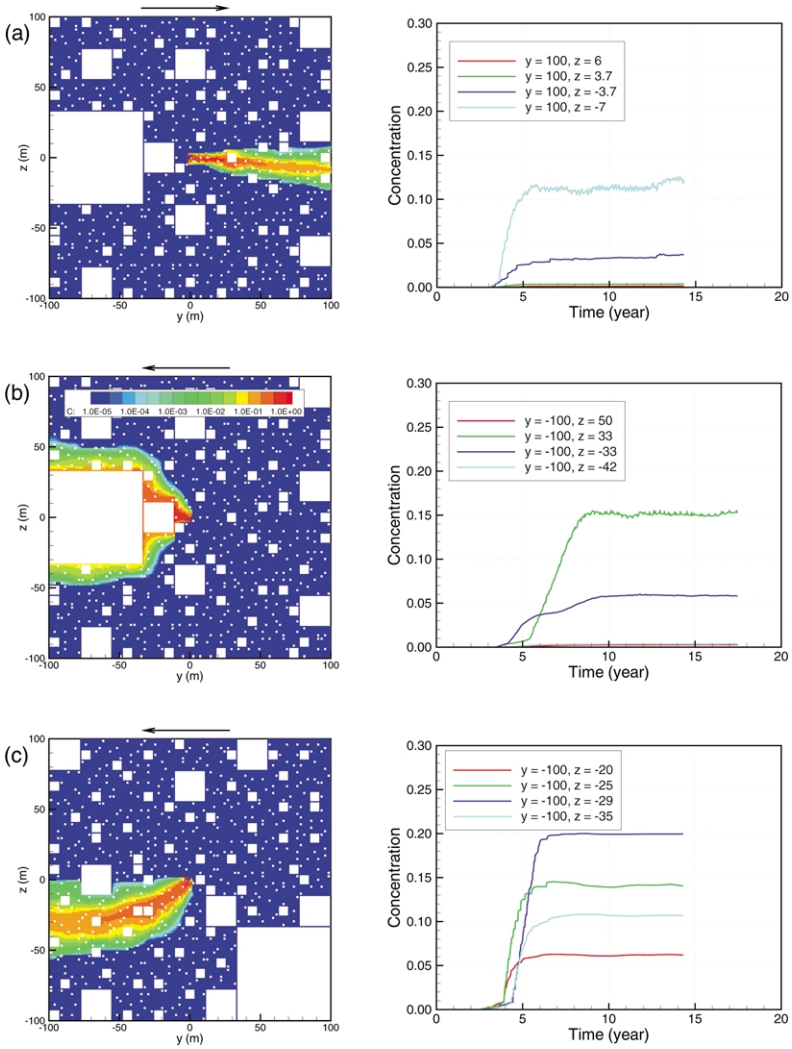

Fig. 16. Steady-state concentration distribution and breakthrough curves at selected points on the downgradient boundary for $N_{sq} = 8$ lattices.

of fractures must converge to a single fracture intersection (e.g. at $y = 33$ m, $z = -33$ m in Fig. 13(a)), resulting in converging flow at one scale and diverging flow at another. Furthermore, this converging-within-diverging pattern can occur at different scales (e.g. the pinch point at $y = -11$ m, $z = -11$ m in Fig. 13(b)), ultimately leading to a great deal of variety in spatial concentration distributions and breakthrough curves.

Interestingly, the breakthrough curves simulated for converging flow fields are much more likely to show oscillations than those resulting from diverging flow fields (e.g. the breakthrough curve at $z = 33$ m in Fig. 13(b)). These oscillations are a numerical effect, arising from instabilities in the mixing of clean and traced water at the few fracture intersections along the flow path as the adaptive gridding scheme adds and deletes nodal points at those intersections to minimize interpolation errors. These numerical instabilities may have natural analogs in the real world, where changes in stress or other non-linearities could subtly alter fracture transmissivities or hydraulic boundary conditions. The point is that for converging flow fields there are not enough fracture intersections for unstable

processes occurring at each one to average out, leading to oscillating breakthrough concentrations.

For larger values of N_{sq}, the convergence of the flow field down to only two fractures becomes less common, but converging–diverging features of the fracture network at different scales still have a strong impact on the tracer flow paths leaving the EDZ. As N_{sq} increases from four to five the fracture network undergoes a transition from having more gaps than fractures to having more fractures than gaps. It is during this transition region that the most variability in fracture network connectivity is possible. Fig. 14 shows examples for $N_{sq} = 4$. In Fig. 14(a), many fracture intersections between the EDZ and the downgradient boundary result in S-shaped breakthrough curves. Fig. 14(a) also shows the phenomenon of crossing breakthrough curves, in which the location with the earliest arrival of tracer does not end up being the location with the maximum tracer concentration. This occurs frequently in the hierarchical fracture networks. In Fig. 14(b), a diverging flow pattern results in uniformly low concentrations. In Fig. 14(c), the flow field shows neither an overall convergence nor divergence. A relatively sharp concentration gradient is apparent across the fracture zone downgradient of the EDZ. Note that several fractures to the left of the EDZ show no concentration increase, as the flow field bypasses them entirely.

Fig. 15 shows examples for $N_{sq} = 5$. In Fig. 15(a), much of the flow through the model is funnelled through the EDZ, and a relatively direct, narrow flow path from the EDZ to the downgradient boundary results in a large value of C_{max}. In Fig. 15(b), there is a narrow plume just downgradient of the EDZ, but then diverging flow following a pinch point causes widening and a decreased C_{max}. The oscillations in the breakthrough curve for $z = 33$ m probably reflect unstable mixing of clean water from the upgradient boundary and traced water from the EDZ at the pinch point. In Fig. 15(c), C_{max} is localized at $11 \text{ m} < z < 22$ m, but the diverging flow field spreads tracer at a lower concentration over a much greater z range. The breakthrough curve at $z = -11$ m shows a double-hump character that suggests there are two primary flow paths from the EDZ, with the slower path having a travel time of about 14 years.

In Fig. 15(a) and (b), the breakthrough curves have a small, early increase in concentration followed some time later by the main concentration front. This low-concentration 'tail' is typical of fracture networks with a relatively direct flow path from the EDZ to the downgradient boundary that is surrounded by many longer flow paths that lead to the same downgradient point. It is a common feature of hierarchical fracture networks.

For large values of N_{sq}, there are often relatively direct paths from the EDZ to the downgradient boundary, but concentration distributions still vary greatly between realizations. Fig. 16 shows examples for $N_{sq} = 8$. Despite the nearly completely filled fracture networks, gaps of all sizes exist so there is a significant variability among realizations. In Fig. 16(a), the flow field shows a gradual convergence to the right of the $L/3$-size gap, which keeps the concentration plume narrow. When the flow direction is reversed (Fig. 16(b)), the plume bifurcates around the $L/3$-size gap and the breakthrough curves feature the low-concentration tails and crossing pattern seen for previous examples. Although the fracture pattern appears to be generally symmetric about $z = 0$, C_{max} is much higher for $z = 33$ m than for $z = -33$ m. This can be explained by the $L/27$-size gap located at $y = -7$ m, $z = -7$ m, which diverts much of the flow upward. In Fig. 16(c), the large gaps in the lower right corner control the overall flow pattern by creating a slightly diverging, diagonal flow field. The diagonal flow is strongly reflected in the concentration plume, despite the fact that the plume never gets close to the gap. If the global character of the flow field were not appreciated during the experimental design, and tracer monitoring only occurred at $z = 0$ (nominally considered downstream of the EDZ), nearly the entire plume would be missed.

4. Discussion and comparison to other studies

A common feature of most of the hierarchical fracture networks studied is that they produce quasi-channelized flow with localized, rapid transport from the EDZ to the downgradient model boundary. Many of the breakthrough curves also show evidence of multiple flow paths, indicating interaction between channels. In general, subtle features of the flow field can produce strong responses in transport phenomena. These features are not unique to hierarchical fracture

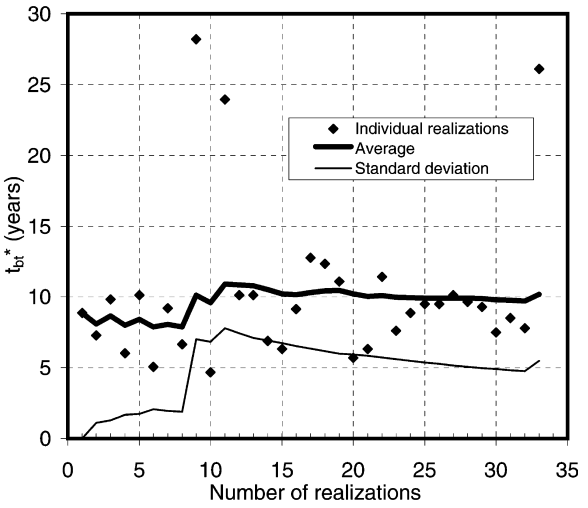

Fig. 17. Normalized breakthrough time t_{bt}^* for $N_{sq} = 5$, illustrating the relationship between individual realizations and averages and standard deviations calculated using increasing numbers of realizations.

networks, but have been noted by authors using a variety of approaches to investigate fracture flow (National Research Council, 1996, Chapter 6). Other findings, particularly the variation of front width described at the end of this section, arise directly from the fractal nature of the hierarchical fracture networks, in which variability occurs on all scales.

It is common for studies using stochastically generated models to consider far more realizations than we consider here, particularly when the variability between realizations is high, as it is for simulation results that depend on a few critical flow paths, such as breakthrough time and EDZ flow. However, we believe enough realizations have been used to make the averages presented meaningful. For example, Fig. 17 shows t_{bt}^* for each realization for $N_{sq} = 5$, along with the average and standard deviation calculated for increasing numbers of realizations. It is clear that despite the large scatter in individual t_{bt}^* values, after 12 realizations the average has stabilized.

We initiate transport by imposing a localized step change in concentration at the EDZ, then follow the resulting tracer plume through the fracture network and examine its arrival at the downgradient model boundary. This procedure reproduces the processes associated with radionuclide release from a nuclear waste repository and the associated natural-gradient tracer test designed to mimic that release. The channelized nature of the flow leads to irregular, difficult-to-predict transport, making any prediction for a single point highly uncertain. Another approach is to introduce tracer all along the upgradient boundary of the model and construct a breakthrough curve by averaging over the entire downgradient boundary of the model (Birkhölzer and Tsang, 1997). This method has the advantage of incorporating the effect of flow paths throughout the medium, but it does not illustrate what is likely to happen during a given tracer test with a localized tracer release point and a limited number of observation points. Others use localized releases of tracer, but primarily focus on spatially averaged breakthrough curves (Grindrod and Impey, 1993; Berkowitz and Scher, 1997; Clemo and Smith, 1997). We have found that looking at average rather than local breakthrough curves is generally not helpful for elucidating the physical processes occurring in the fracture network. Moreover, it is often misleading as to the range of responses expected in an actual field experiment with only a few observation points, precisely because the critical fast flow paths that produce the earliest tracer arrivals are not representative of the average behavior of the medium. A preferable situation is to be able to monitor over a spatially extensive region, such as an underground drift or a surface exposure such as a cliff face. Then both local and average predictions can be made and compared to local and average observations, respectively.

The finding that front thickness $\Delta y \approx y$ for a large range of fractal dimensions (Fig. 11(b)) may seem surprising in view of numerous authors' suggestions that the commonly observed scale-dependence of dispersivity (Gelhar et al., 1985) can be explained as a consequence of the fractal dimension of the tracer flow path (Tyler and Wheatcraft, 1992 and references therein). In the conventional ADE with constant values of groundwater velocity and dispersivity α_L, front thickness depends on time according to $\Delta y \sim (\alpha_L t)^{1/2}$ and on distance travelled according to $\Delta y \sim (\alpha_L y)^{1/2}$. In contrast, for scale-dependent or anomalous dispersion, $\Delta y \sim t^r$ and $\Delta y \sim y^r$, where $r > 1/2$. To preserve the connection with the conventional ADE, a variable dispersivity α_m is introduced so that $\Delta y \sim (\alpha_m t)^{1/2}$ with $\alpha_m \sim t^{2r-1}$ and $\Delta y \sim (\alpha_m y)^{1/2}$ with $\alpha_m \sim y^{2r-1}$. To explain this phenomenon with

a fractal model, an expression for the power r as a function of fractal dimension D must be derived. For example, Wheatcraft and Tyler (1988) obtain $\alpha_m \sim y^{2D-1}$ ($r = D$), based on a random walk over a set of fractal stream tubes.

In the present studies, we find $\Delta y \sim y$, which requires $\alpha_m \sim y$ or $r = 1$, which is the dispersivity dependence for a stratified aquifer (Mercado, 1967). Neretnieks (1983) recognized that this relationship applies to channelized flow as well. It is natural for heterogeneous models to produce channelized flow at one scale, but Ross (1986) points out that fractal media have the unique capability of producing channelized flow at all scales: at any experimental scale, there are always a few fractures that are nearly as large as the experimental scale; these provide quasi-independent channels through which most of the flow occurs; as the experimental scale increases, longer fractures come into play and channeling is maintained. This explanation is consistent with the finding that $\Delta y \approx y$ independent of fractal dimension, for a range of y values between 5 and 100 m.

However, it must be noted that the expression $\Delta y \approx y$ produces only a roughly approximate fit to the numerical results and there is a great deal of scatter around it both for observations at $y = 100$ m (Fig. 11(b)) and for smaller values of y (not shown). This is not surprising since using the conventional ADE with dispersivity represented as a function of time or space to account for scale-dependent dispersivity is an ad hoc approach. In fact, Berkowitz and Scher (1995) are able to prove that using $\alpha_m(t)$ leads to quantifiably incorrect solutions for the anomalous dispersion caused by differential advection through a highly heterogeneous medium. Cushman (1991) treats transport in a fractal medium rigorously and obtains a non-local integrodifferential governing equation in place of the conventional ADE. In other words, transport at a given point depends on the history of concentration at that point as well as concentrations elsewhere in space.

5. Summary and conclusions

We have generated hierarchical fracture networks with well-defined fractal dimensions and simulated single-well pump tests and natural-gradient tracer tests through them. By examining multiple realizations we have looked for trends that describe the variation of transport with fractal dimension and features that are unique to particular fracture network geometries. The studies attempt to illustrate the range of possible behavior that might be obtained during field tracer tests conducted in hierarchically fractured rock and provide insights into how to interpret field responses. Some specific findings are presented below followed by more general concluding remarks.

1. As the number of filled squares N_{sq} in the random Sierpinski lattices increases, the fractal dimension of the fracture network D increases according to Eq. (5).
2. The generalized radial flow dimension n obtained during a well test also increases with N_{sq}. For all fracture networks, $n < D$. The variability of n and D among different realizations is small.
3. For the linear flow field obtained during a natural-gradient tracer test, the effective transmissivity of the fracture network is well fit by the relationship $\ln(T_{eff}/T_0) = (N_{sq}/4)^2$, where T_0 is the transmissivity of a fracture network with $N_{sq} = 0$. Given the smooth relationships between N_{sq}, D, and n, simple analytical expressions could also be written for $T_{eff}(D)$ and $T_{eff}(n)$.
4. During natural-gradient tracer tests, the relative amount of flow through the EDZ (the tracer source) tends to increase with fractal dimension, as smaller gaps in the fracture network make it less likely that the EDZ will be bypassed by the primary flow channels.
5. During tracer tests, channelized flow tends to produce early, localized tracer breakthroughs, but some interaction between channels is also apparent, as breakthrough curves show evidence of multiple flow paths arriving at a given point.
6. Normalized breakthrough time t^*_{bt} decreases as fractal dimension increases, due to the addition of more and more direct flow paths through the model.
7. Front width Δy is independent of fractal dimension over the range $3 \leq N_{sq} \leq 8$ and is approximately equal to the distance travelled by the front. This linear dependence is consistent with channeling that occurs over a range of length scales, which is expected for a hierarchical fracture network.

8. Maximum concentration at the downgradient boundary C_{max} is quite low compared to the unit concentration maintained at the EDZ and C_{max} shows only a slight increase with fractal dimension for $N_{sq} \leq 8$. This suggests that even for dense fracture networks the occasional gaps disrupt and disorganize the flow pattern, leading to low values of C_{max}.

Geometry and flow-related properties D, n, and T_{eff} represent average behavior over the whole fracture network and thus show little variability between realizations for a given N_{sq}. Consequently, the averaged relationships for D, n, and T_{eff} as a function of N_{sq} apply quite well to all realizations. In contrast, transport-related properties Q_{EDZ}, t_{bt}, Δt, and C_{max} are controlled by a relatively few fractures and consequently are very sensitive to subtle variations in the fracture network and the flow field. Because of the hierarchical fracture network structure, flow field variations occur at all scales. In particular, the existence of gaps of all sizes means that the converging–diverging pattern associated with pinch points occurs at all scales. Large-scale flow field features control the overall direction of the tracer plume and whether it broadens or remains narrow. At smaller scales, flow can be focused toward the EDZ or largely bypass it, strongly affecting the resulting tracer plume. Consequently, there is a great deal of variability in transport properties among realizations, which must be appreciated when looking for trends associated with fractal dimension.

At a fractal dimension of $D = 1.5$, there is a transition from networks with more gaps than fractures ($N_{sq} \leq 4$) to networks with more fractures than gaps ($N_{sq} \geq 5$). This is where the greatest variability in fracture network geometry occurs, leading to the biggest uncertainty in flow and transport properties. However, even for fractal dimensions near $D = 2$ there is still a very large variability among transport simulation results for different realizations. Moreover, within a given realization there is also a great deal of variability, as evidenced by the large values of Δy and small values of C_{max}. These findings are consistent with and may partially explain the large variability in the experimental results observed at fractured rock field sites (Olsson, 1992; Mauldon et al., 1993; Uchida et al., 1993; Hsieh and Shapiro, 1996; Karasaki et al., 2000).

Acknowledgements

We thank Don Vasco and Chin-Fu Tsang of LBNL and two anonymous reviewers for their comments. This work has been supported by Japan Nuclear Cycle Development Institute (JNC) through the US Department of Energy Contract No. DE-AC03-76SF00098.

References

Barker, J.A., 1988. A generalized radial flow model for hydraulic tests in fractured rock. Water Resources Research 24 (10), 1796–1804.

Barton, C.C., Hsieh, P.A., 1989. Physical and hydrologic-flow properties of fractures. 28th International Geological Congress Field Trip Guidebook T385, American Geophysical Union, Washington, DC.

Berkowitz, B., Scher, H., 1995. On characterization of anomalous dispersion in porous and fractured media. Water Resources Research 31 (6), 1461–1466.

Berkowitz, B., Scher, H., 1997. Anomalous transport in random fracture networks. Physical Review Letters 79 (20), 4038–4041.

Birkhölzer, J., Karasaki, K., 1996. FMGN, RENUMN, POLY, TRIPOLY: Suite of programs for calculating and analyzing flow and transport in fracture networks embedded in porous matrix blocks. Rep. LBNL-39387, Lawrence Berkeley National Laboratory, Berkeley, California.

Birkhölzer, J., Tsang, C.-F., 1997. Solute channeling in unsaturated heterogeneous porous media. Water Resources Research 33 (10), 2221–2238.

Clemo, T., Smith, L., 1997. A hierarchical model for solute transport in fractured media. Water Resources Research 33 (8), 173–1783.

Cushman, J.H., 1991. On diffusion in fractal porous media. Water Resources Research 27 (4), 643–644.

Doughty, C., Karasaki, K., 1999. Using an effective continuum model for flow and transport in fractured rock: the H-12 flow comparison. Rep. LBNL-44966, Lawrence Berkeley National Laboratory, Berkeley, California.

Doughty, C., Karasaki, K., 2000. Using Sierpinski lattices to study flow and transport in hierarchically fractured rock. Rep. LBNL-47030, Lawrence Berkeley National Laboratory, Berkeley, California.

Gelhar, L.W.A., Mantoglou, C.W., Rehfeldt, K.R., 1985. A review of field scale physical solute transport processes in saturated and unsaturated porous media. Rep. EA-4190, Electric Power Research Institute, Palo Alto, California.

Grindrod, P., Impey, M.D., 1993. Channeling and fickian dispersion in fractal simulated porous media. Water Resources Research 29 (12), 4077–4089.

Hsieh, P.A., Shapiro, A.M., 1996. Hydraulic characteristics of fractured bedrock underlying the FSE well field at the Mirror Lake Site, Grafton County, New Hampshire. In: Morganwalp, D.W.,

Aronson, D.A. (Eds.). US Geological Survey Toxic Substances Hydrology Program—Proceedings of the Technical Meeting, Colorado Springs, Colorado, September 20–24, 1993. US Geological Survey of Water Resources Investigation Report, 94-4015, 1, pp. 127–130.

Karasaki, K., 1987. Well test analysis in fractured media. PhD Thesis, Department of Material Science and Mineral Engineering, University of California, Berkeley, Rep. LBL-21442, Lawrence Berkeley Laboratory, Berkeley, California.

Karasaki, K., 1987. A new advection–dispersion code for calculating transport in fracture networks. Earth Sciences Division 1986 annual report, Rep. LBL-22090, Lawrence Berkeley Laboratory, Berkeley, California, pp. 55–58.

Karasaki, K., Freifeld, B., Cohen, A., Grossenbacher, K., Cook, P., Vasco, D., 2000. A multidisciplinary fractured rock characterization study at Raymond field site, Raymond, California. Journal of Hydrology 236 (1–2), 17–34.

Mandlebrot, B.B., 1982. The Fractal Geometry of Nature. Freeman, San Francisco.

Mauldon, A.D., Karasaki, K., Martel, S.J., Long, J.C.S., Landsfield, M., Mensch, A., 1993. An inverse technique for developing models for fluid flow in fracture systems using simulated annealing. Water Resources Research 29 (11), 3775–3789.

Mercado, A., 1967. The spreading pattern of injected water in a permeability-stratified aquifer, vol. 72. IAHS AISH Publication, Gentbrugge, Belgium pp. 23–36.

Moreno, L., Tsang, C.-F., 1994. Flow channeling in strongly heterogeneous porous media: a numerical study. Water Resources Research 30 (5), 1421–1430.

National Research Council (Committee on Fracture Characterization and Fluid Flow), 1996. Rock Fractures and Fluid Flow: Contemporary Understanding and Applications. National Academy Press, Washington, DC.

Neretnieks, I., 1983. A note on fracture flow dispersion mechanisms in the ground. Water Resources Research 19 (2), 364–370.

Olsson, O., 1992. Site characterization and validation—final report: Stripa project. Technical Report 92-22, Swedish Nuclear Fuel and Waste Management Co. (SKB), Stockholm.

Ott, E., 1993. Chaos in Dynamical Systems. Cambridge University Press, New York, Chapters 3 and 9.

Oyamada, K., Ikeda, T., 1999. Uncertainty analysis on hydrologic modeling in heterogeneous media (CORE Collaborative Study). Rep. TJ1400 99-023, Japan Nuclear Fuel Cycle Development Institute.

Polek, J.M., 1990. Studies of the hydraulic behavior of hierarchically fractured rock geometries. MS Thesis, Department of Material Science and Mineral Engineering, University of California, Berkeley, Rep. LBL-28612, Lawrence Berkeley Laboratory, Berkeley, California.

Press, W.H., Flannery, B.P., Teukolsky, S.A., Vetterling, W.T., 1986. Numerical Recipes: The Art of Scientific Computing. Cambridge University Press, New York.

Ross, B., 1986. Dispersion in fractal fracture networks. Water Resources Research 22 (5), 823–827.

Sahimi, M., 1993. Flow phenomena in rocks: From continuum models to fractals, percolation, cellular automata and simulated annealing. Reviews of Modern Physics 65 (4), 1393–1534.

Sahimi, M., Robertson, M.C., Sammis, C.G., 1993. Fractal distribution of earthquake hypocenters and its relation to fault patterns and percolation. Physical Review Letters 70 (14), 2186–2189.

Sawada, A., Shiotsuki, M., Oyamada, K., Takase, H., 1999. Study of flow model comparison in fractured rock. Proceedings of the 30th Symposium of Rock Mechanics, Japan Society of Civil Engineering, Tokyo, January 26–27.

Segan, S., Karasaki, K., 1993. TRINET: A flow and transport code for fracture networks—user's manual and tutorial. Rep. LBL-34839, Lawrence Berkeley Laboratory, Berkeley, California.

Theis, C.V., 1935. The relation between the lowering of the piezometric surface and the rate and duration of discharge of a well using ground-water storage. Transactions of American Geophysical Union 16, 519–524.

Turcotte, D.L., 1992. Fractals and Chaos in Geology and Geophysics. Cambridge University Press, New York.

Tyler, S.W., Wheatcraft, S.W., 1992. Reply. Water Resources Research 28 (5), 1487–1490.

Uchida, M., Sawada, A., 1995. Discrete fracture network modelling of tracer migration experiments at the Kamaishi mine. Material Research Society Proceedings 353, 1995.

Uchida, M., Doe, T.W., Dershowitz, W., Wallman, P., 1993. Simulation of fracture flow to the Kamaishi validation drift. Proceedings of the Fourth Annual International Conference of High Level Radioactive Waste Management, Las Vegas, Nevada, American Nuclear Society, pp. 437–442.

Wheatcraft, S.W., Tyler, S.W., 1988. An explanation of scale-dependent dispersivity in heterogeneous aquifers using concepts of fractal geometry. Water Resources Research 24 (4), 566–578.